relatively imperfect crystals of α-aluminum oxide, about 0·2 mm thick. The phases of the reflections are, of course, well known for both materials.

To achieve adequate resolution, a microfocus divergent X-ray beam was used. The X-ray source was a Cu K target; the focus was about 40 μm in diameter. At the take-off angles used in this work (4 to 8°), the effective focal spot was about 40 × 5 μm. The specimen crystals were oriented so that the smaller dimension determined the resolution along the two-beam reflection lines shown in Fig. 6(*a*) and (*b*). The source-to-crystal distance was 80 mm; the specimen-to-film distance was 1650 mm. The latter path was evacuated.

About 25 three-beam interactions in germanium and aluminum have been recorded photographically, using Kodak Type A film.* Fig. 6(*a*) and (*b*) illustrates the results obtained and shows two-beam Cu $K\alpha_1$ and α_2 $(1\bar{1}2)$ reflection lines. The three-beam interaction regions are near the centers of the photographs. In Fig. 6(*a*) (positive phase) there is no significant difference between the intensities recorded to the left and right of the three-beam region. The left–right intensity differences calculated for negative phases are clearly displayed in Fig. 6(*b*). In fewer than half of the photographs were the positive–negative intensity differences too small to permit definitive phase assignments. Most of these difficulties appeared to be caused by our selection of relatively unfavorable triplets for study, *i.e.* cases in which the magnitudes of the three F's differed widely from one another. None of the photographs, however, indicated phases at variance with the known, correct ones.

* The photographs were taken by Mr Po Wen Wang, to whom the author is deeply grateful.

Summary

The phases of X-ray reflections from single crystals are not lost when three-beam simultaneous diffraction occurs. They may be determined by analyzing the distribution of the diffracted intensities about the three-beam point, under the conditions outlined in the preceding sections. It is not yet possible to indicate the extent to which the phase-determining methods described above can be applied to the 'mosaic' crystals usually used in crystal structure analysis. Our experience with relatively imperfect aluminum oxide crystals shows that the crystals need not be ideally perfect. Additional work with highly imperfect crystals is needed. The strictly collimated and highly intense X-ray beams available from synchrotron sources appear to be ideally suited for investigations of this sort.

References

BATTERMAN, B. W. & COLE, H. (1964). *Rev. Mod. Phys.* **36**, 681–717.
ECKSTEIN, H. (1949). Private communication to Lipscomb (1949).
EWALD, P. P. (1916). *Ann. Phys. (Leipzig)*, **49**, 1–38.
EWALD, P. P. (1917). *Ann. Phys. (Leipzig)*, **54**, 519–597.
EWALD, P. P. & HÉNO, Y. (1968). *Acta Cryst.* A**24**, 1–15.
FANKUCHEN, I. (1949). Private communication; also quoted by Lipscomb (1949).
HART, M. & LANG, A. P. (1961). *Phys. Rev. Lett.* **7**, 120–122.
JAMES, R. W. (1963). *Solid State Phys.* **15**, 53–220.
KAMBE, K. (1957). *J. Phys. Soc. Jpn*, **12**, 13–31.
LIPSCOMB, W. N. (1949). *Acta Cryst.* **2**, 193–194.
MIYAKE, S. & KAMBE, K. (1954). *Acta Cryst.* **7**, 218–220.
SCHWARTZ, L. H. & COHEN, J. B. (1977). *Diffraction from Materials*, ch. 8. New York: Academic Press.

Acta Cryst. (1979). A**35**, 21–28

Computer-Simulation Methods in X-ray Topography*

BY J. R. PATEL

Bell Laboratories, Murray Hill, NJ 07974, *USA*

(*Received* 22 *May* 1978; *accepted* 13 *September* 1978)

Abstract

Complex diffraction contrast features on X-ray topographs are often difficult to interpret by simple arguments. In such cases computer-simulation methods have frequently proved useful in understanding the observed contrast features and in elucidating the nature of the defect involved. The application of computer-simulation methods for interpreting X-ray diffraction contrast at planar and line defects in crystals is outlined.

* This paper was presented, by invitation, at the ACA Dynamical Diffraction Symposium held at the University of Oklahoma, 22 March 1978, honoring Paul P. Ewald on the occasion of his ninetieth birthday.

There are many instances in X-ray topography where detailed analyses of the various complex contrast effects observed are necessary. In such cases it would

0567-7394/79/010021-08$01.00

be useful to have a simple simulation technique where one could vary the various diffraction and defect parameters to match the desired contrast features and thus unambiguously establish the nature of the defects observed. Such simulation methods have long been widely used in transmission electron microscopy, where the two-beam dynamical equations using plane waves and the column approximation allow rapid computation of the contrast features from defects. Such techniques were applied by Head, Humble, Clarebrough, Forwood & Morton (1973) and co-workers and subsequently refined by various groups, for example Bullough, Maher & Perrin (1971). For X-ray topography computer simulations have not been as widely used owing in large measure to the complexity of the calculations. Because of the large Bragg angles for X-rays the column approximation does not apply. Furthermore, as pointed out by Kato (Azaroff, Kaplow, Kato, Weiss, Wilson & Young, 1974), the plane-wave treatment is inadequate and the spherical-wave theory must be used. Nevertheless, some attempts have been made to simulate topographs, notably by Balibar & Authier (1967) for dislocations. These calculations have been refined by Epelboin (1974). Simulations of stacking faults have been published by Authier & Patel (1975) and with extensive refinements by Wonsiewicz & Patel (1976) and finally other planar defects such as twins and grain boundaries have been simulated by Katagawa, Ishikawa & Kato (1975). In this paper we shall deal mainly with planar defects with only a brief mention of line defects which are covered in detail in a following paper (Epelboin, 1979). Simulations of dislocation images for the plane-wave case have been given by Ishida, Miyamoto & Kohra (1976) and for the Bragg case by Bedynska (1973). These cases will not be discussed in this paper, which is confined mainly to the transmission geometry.

Theory

The dynamical diffraction problem of a crystal with a stacking fault has been treated by Kato, Katagawa & Usami (1967) and Authier & Sauvage (1966). In the present work we will use the treatment of Authier (1968), which considers all of the interference terms and includes absorption. The actual results of the dynamical-theory calculations are lengthy and involved. Their application has been treated in detail by Authier & Patel (1975). Here we outline the nature of the various contributions to the intensity of the section pattern of a stacking fault and highlight the important parameters. Consider (as shown in Fig. 1) the various contributions to the intensity at a point P on the exit surface of a crystal with a stacking fault. The wavefield (1) travelling in crystal I crosses the fault and travels in crystal II and arrives at P without any interbranch scattering. The newly created wavefield (2), which travels in crystal I in the direction shown but which suffers interbranch scattering at the fault surface, also contributes to the intensity at P. Finally, we have interference between the waves that have and have not suffered interbranch scattering and these will also contribute to the intensity at P. The three contributions have been summarized by Patel & Authier (1975):

$$I_1 = I_{\text{perf}}(1 - A \sin^2 \delta/2). \quad (1)$$

The contribution to the intensity in equation (1) is due to the original wavefields; A involves various diffraction and geometrical parameters and $\delta = -2\pi\mathbf{h}.\mathbf{u}$, where $\mathbf{h}$ is the reciprocal-lattice vector and $\mathbf{u}$ is the fault vector. if $\mathbf{u} = 0$, $\delta = 0$ and $I_1 = I_{\text{perf}}$. The interference between the newly created wavefields is given by

$$I_2 = B \sin^2 \delta/2. \quad (2)$$

Finally, the interference between the old and newly created wavefields can be represented by

$$I_3 = C \sin^2 \delta/2 + D \sin \delta/2. \quad (3)$$

It is only the last term in equation (3) that can distinguish between the sign of the fault vector $\pm\mathbf{u}$. For appreciable contribution from this term, D, which depends on absorption, must be large. Hence in cases where the absorption factor μd is small we will not be able to distinguish between $\pm\mathbf{u}$. The details of the computation procedure for evaluating the intensity at each point on the section pattern have been given by Wonsiewicz & Patel (1976). Briefly, we set up a grid of points on the section pattern where I_1, I_2, and I_3 must be calculated. We convert the total intensity to a photographic density through the relation $\rho = \gamma \log I + C$, where γ is the film response. Next the data are packed and written on magnetic tape and the calculation moves on to the next line of points. The tape is used to drive a facsimile device which is capable of writing 10, 20, or 40 points mm^{-1} by rotating a photographic film on a drum past a light beam whose intensity is controlled by the I values on the magnetic tape.

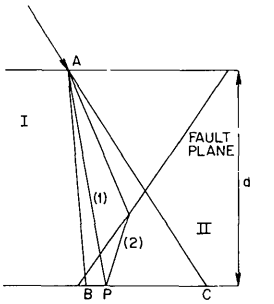

Fig. 1. X-ray paths in the crystal showing contributions to the intensity at point P on the exit surface.

Results

I. *Section topographs – asymmetric faults*

An example of a simulation of a silicon crystal with a stacking fault taken from the work of Wonsiewicz & Patel (1976) is shown in Fig. 2(*a*) and (*b*). Note the characteristic hour-glass shape of the section pattern of a crystal with a stacking fault. For the same **h** the contrast of the fringe at the exit surface *FH* changes from white to black for extrinsic and intrinsic faults respectively (Fig. 2*a* and *b*). In simulations not shown in Fig. 2 the contrast reverses when the fault vector is reversed (−**h**) for the respective faults. Thus knowing the fault geometry and the diffraction conditions, we can unambiguously determine the nature of the fault from its section pattern.

II. *Traverse topographs – asymmetric faults*

More commonly in X-ray topography one uses traverse topographs where the pattern observed on section topographs is integrated. We carry out such an integration of Fig. 2(*a*) along lines parallel to *FH*, which is the trace of the fault on the exit surface and also the apparent translation of the section pattern during the traverse of the X-ray beam across the fault. The result is shown in Fig. 2(*c*). For the extrinsic fault the first fringe is black in contrast to the white fringe on the corresponding section in Fig. 2(*a*). Thus traverse topographs may not in general be able to discriminate between the fault type since the first fringe is black for both extrinsic and intrinsic faults, Fig. 2(*c*) and (*d*). If we choose the −**h** geometry, the situation is normal and the fault can be distinguished, on the traverse topograph, the first fringe being black for extrinsic and white for an intrinsic fault. Evidently, the high intensity in the vicinity of *H* in Fig. 2(*a*) overwhelms the light fringe along *FH* and gives rise to the apparent anomaly between the section and traverse patterns.

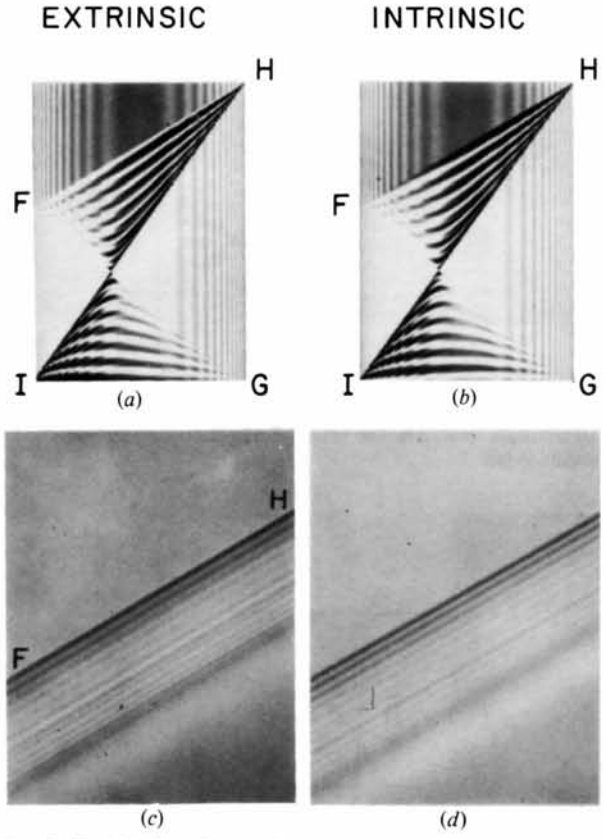

Fig. 2. Simulated section and traverse topographs of asymmetric faults in a (111) silicon crystal; Cu $K\alpha_1$ radiation, $\mu d = 3{\cdot}7$, $\mathbf{h} = \bar{1}1\bar{1}$, $\mathbf{u} = 1\bar{1}\bar{1}$. (*a*) +**h**, −**u**, extrinsic fault; (*b*) +**h**, +**u**, intrinsic fault; (*c*) traverse corresponding to section topograph in (*a*); (*d*) traverse corresponding to section in (*b*) from Wonsiewicz & Patel (1976).

III. *Experiment – asymmetric faults*

An experimental section and traverse topograph of an extrinsic fault in silicon corresponding to the simulations in Fig. 2 is shown in Fig. 3. All of the general features of the simulation are observed experimentally. Note that the white fringe at *FH* on the exit surface in Fig. 3(*a*) appears dark on the corresponding traverse pattern Fig. 3(*b*). The broad white contrast on the entrance surface of the transverse pattern Fig. 3(*b*) bears strong resemblance to the corresponding regions on the simulation (Fig. 2*c*).

IV. *Simulation – symmetric faults*

Under the supposition that the asymmetric geometry of the fault might be responsible for the apparent anomaly observed, Wonsiewicz & Patel (1976) simulated symmetric faults whose traces on the surfaces are parallel to the traverse direction. Such a geometry is realized when the crystal surface is (100) and the fault and diffraction planes are {111}. Under these conditions the simulated section and traverse patterns are normal, as shown in Fig. 4(*a*) and (*b*), where the white fringe at the exit surface on the traverse Fig. 4(*b*) corresponds to the white fringe on the section Fig. 4(*a*). Another condition under which the anomaly should vanish is for anomalous transmission where the absorption factor is large $\mu d \simeq 10$. It is apparent from Fig. 5(*d*), which simulates an asymmetric fault with high μd (=10), why this should be so. The large intensity at the margin *IH* in Fig. 5(*a*)–(*c*) has vanished for $\mu d = 10$. To summarize, we expect that for symmetric faults and normal absorption factors values of $\mu d \approx 3$, the anomaly between the section and traverse patterns should vanish. Furthermore, the anomaly should also vanish for any fault when $\mu d \approx 10$.

V. *Experiment and simulation – symmetric faults*

Recently Patel, Wonsiewicz & Freeland (1979) have tested the above hypothesis in (100) crystals of silicon, in which faults were introduced in a controlled manner by suitable heat treatment (Patel, Jackson & Reiss, 1977). The results are shown in Fig. 6, where, for $\mu d = 3{\cdot}8$, the fault section pattern Fig. 6(*a*) shows a white fringe while the corresponding fringe on the traverse is black (Fig. 6*b*). In this case the simulation of the traverse pattern does not reflect this anomaly as shown in Fig. 6(*c*) and (*d*). This is an unexpected result. So far even for asymmetric faults there has been no discrepancy between the simulated and experimental traverse patterns. It is only the intermediary image, presumably of the dislocation at the fault edge and visible on the left-hand side in the region outside the fault (Fig. 6*b*), that indicates that the first fringe is white, while along the entrance surface of the fault this white fringe is suppressed. Examination of the section pattern Fig. 6(*a*) shows that the region in the vicinity of the intersection of the incident X-ray beam with the fault surface is intensely dark. The simulation Fig. 6(*c*) does not show this exaggerated dark region. All of the other features, such as the flat fringes in the hour-glass pattern, agree quite well with the simulation. When $\mu d \approx 8$ this anomaly persists as shown in Fig. 7. Again, the high intensity at *H* overrides the first white fringe. This result was not expected from the simulated section for an asymmetric fault at $\mu d \simeq 10$ (Fig. 5*d*).

Simulations of twins and grain boundaries

Katagawa and co-workers (in preparation), using the theoretical approach outlined earlier, have simulated both twins and grain boundaries. For a Dauphiné twin in quartz no displacement **u** is involved; only the structure factors in the two crystals separated by the fault are different. Simulations of Dauphiné twins shown in Fig. 8 were produced in large format on a teleprinter and reduced to give the fine detail observed. The experimental section topograph of a Dauphiné twin is on the extreme left, to the right there are various simulations corresponding to deliberately induced displacements Δ along the twin plane. Note that $\Delta = 0$ gives the pattern for an ideal twin, which does not correspond to the experiment. Perhaps the simulation in which the two halves of the crystal are displaced by $\Delta = \pi/4$ corresponds most closely with the observation (when $\Delta = 2\pi$, the two halves of the crystal are displaced by a lattice distance). Note that the experiment again clearly shows more intensity along the intersection of the fault and the incident X-ray beam. Similar observations were pointed out earlier for the case of stacking faults.

For an ideal tilt boundary again the displacement $\Delta = 0$. However the tilt can vary and is expressed by the factor $x = \Delta\theta/\Delta\theta_B$, where $\Delta\theta_B$ is the half-width of the Bragg reflection and $\Delta\theta$ the boundary tilt. Simulations of such tilt boundaries are shown in Fig. 9. The degree to which the observed pattern changes for small changes in $\Delta\theta$ is remarkable and makes the topographic method very sensitive to tilts which are fractions of the half-width of the Bragg reflection.

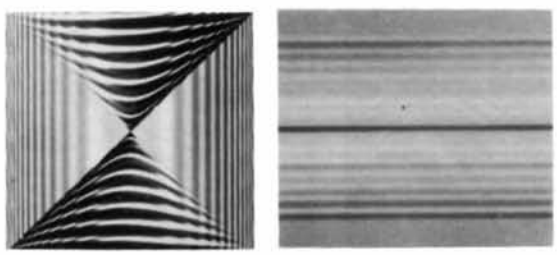

(*a*) (*b*)

Fig. 4. Simulated section patterns of symmetric faults in a (100) silicon crystal; Cu $K\alpha_1$ radiation, $\mu d = 3{\cdot}7$, $\mathbf{h} = \bar{1}1\bar{1}$, $\mathbf{u} = 1\bar{1}\bar{1}$. (*a*) Extrinsic fault, $+\mathbf{h}$, $-\mathbf{u}$; (*b*) traverse pattern corresponding to section in (*a*).

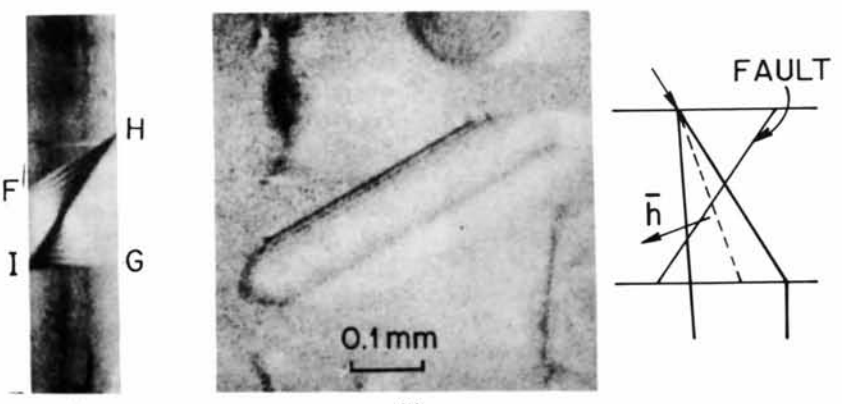

(*a*) (*b*)

Fig. 3. Experimental topographs; Cu $K\alpha$ radiation, $\mu d = 3{\cdot}7$. (*a*) Section topograph, $+\mathbf{h} = \bar{1}1\bar{1}$. (*cf.* simulation Fig. 2*a*); (*b*) traverse topograph corresponding to (*a*) (*cf.* simulation in Fig. 2*c*).

Simulation of dislocations

The first simulations of dislocations were attempted by Balibar & Authier (1967). These calculations were performed by integrating Takagi's (1962) equations in a crystal containing a dislocation. Using isotropic elasticity theory, Balibar & Authier (1967) were able to reproduce the major features observed experimentally. In Fig. 10 we show the progress of such simulations. Fig. 10(*a*) is the experimental section topograph of a dislocation. Fig. 10(*b*) shows the first hand simulation of the defect in (*a*). Subsequent refinements by Y. Epelboin led finally to the simulation in Fig. 10(*d*) performed on an IBM experimental teleprinter. There is little doubt that the calculated topograph faithfully reproduces all of the experimentally observed fringe details. However, we again notice that in the region of the direct image *D* the simulations underestimate the observed intensity. In this case the decreased intensity

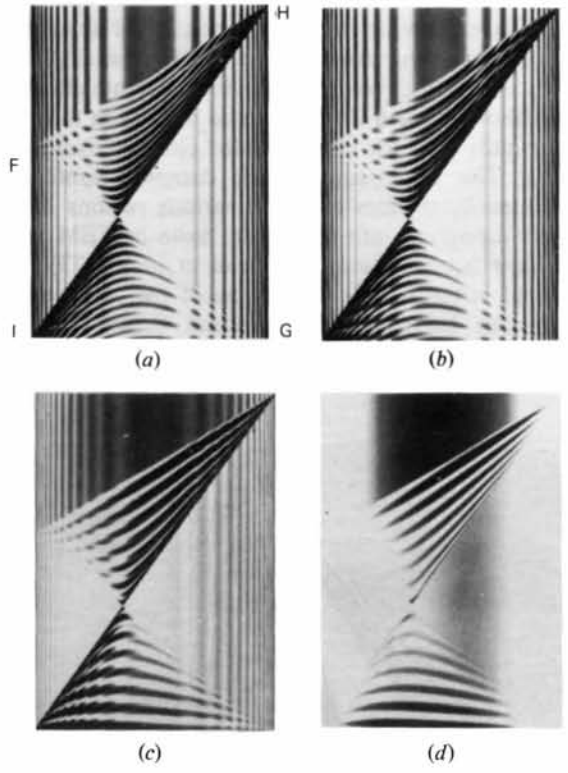

Fig. 5. Simulated section topograph illustrating the effect of absorption on the fringe pattern; Cu $K\alpha_1$ radiation, $\mathbf{h} = 111$, $\mathbf{u} = 1\bar{1}\bar{1}$. The crystal thickness is held at 0·26 mm and μ is varied. (*a*) $\mu d = 0$; (*b*) $\mu d = 1{\cdot}0$; (*c*) $\mu d = 3{\cdot}7$; (*d*) $\mu d = 10{\cdot}0$.

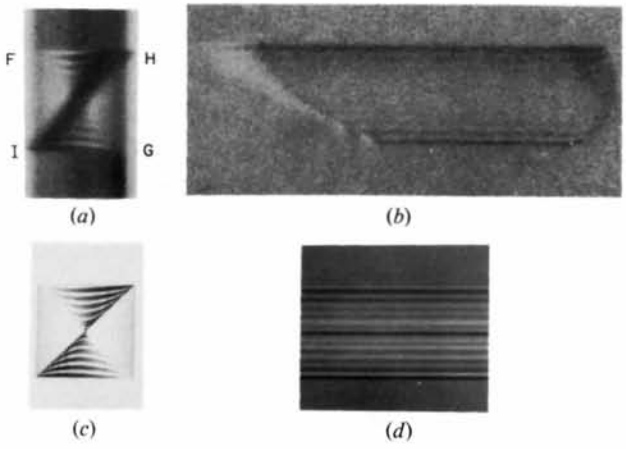

Fig. 6. (*a*) Experimental section and (*b*) traverse topograph of extrinsic symmetric fault in silicon; $+\mathbf{h}$, $-\mathbf{u}$, Cu $K\alpha_1$ radiation, $\mathbf{h} = 111$, $\mu d = 3{\cdot}8$. (*c*) and (*d*): computer simulations of the faults in (*a*) and (*b*).

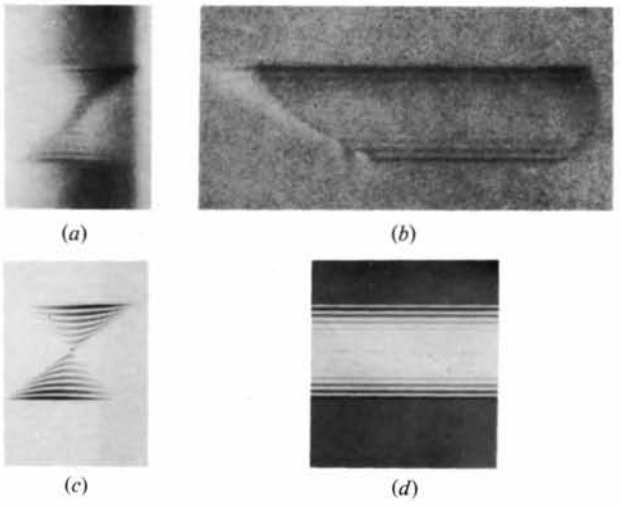

Fig. 7. (*a*) Experimental section and (*b*) traverse topograph of the fault in Fig. 8; Fe $K\alpha_1$ radiation, $\mu d = 8$, $\mathbf{h} = 111$. (*c*) and (*d*): computer simulations of faults in (*a*) and (*b*).

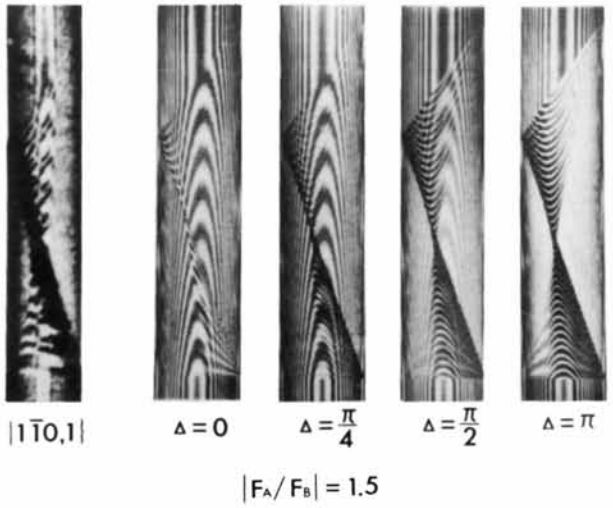

Fig. 8. Experimental section pattern of Dauphiné twin in quartz compared with simulation with and without a shift Δ along the twin plane (after Katagawa *et al.*, 1975).

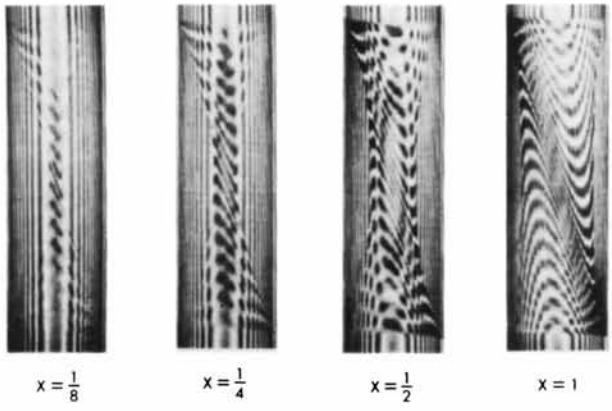

Fig. 9. Simulations of tilt boundaries with increasing misorientation (after Katagawa *et al.*, 1975).

is due to the computation procedure where the use of a finite step size results in neglect of intensity near the margins of the Bormann fan.

Discussion and summary

So far developments in X-ray topographic simulation methods have progressed to a point where reliable high-quality images can be obtained with moderate effort. In all likelihood there will be increased activity in this area as demands arise for more detailed characterization of defects. The advantages of the complete simulation over intensity profiles taken at various regions of the section topograph are similar to those in TEM work and have been outlined by Head *et al.* (1973). The principal virtue is that all aspects of the X-ray topograph can be compared in great detail with the theoretical image.

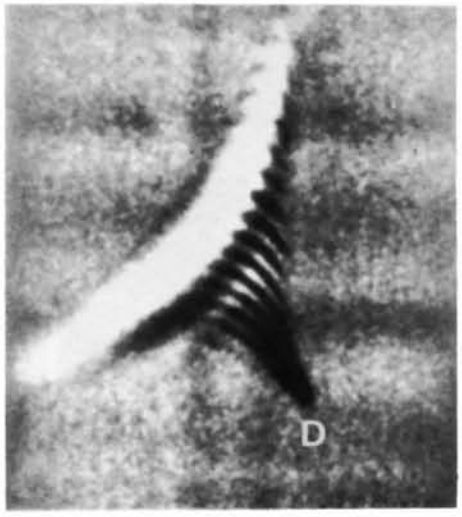

(*a*)

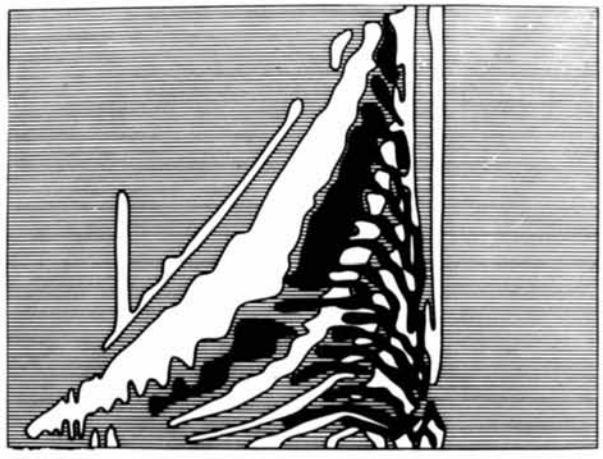

(*b*)

(*c*)

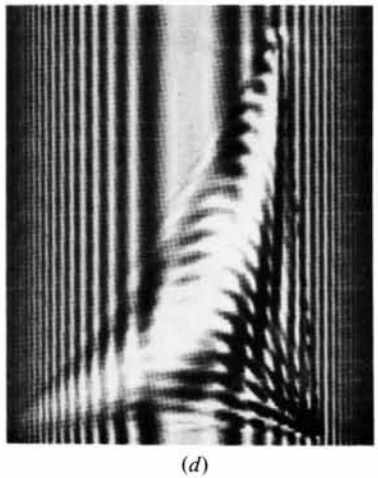

(*d*)

Fig. 10. Observed and simulated section topographs of a dislocation: (*a*) experimental and (*b*) simulated topograph (Balibar & Authier, 1967): (*c*) computer simulation of the same defect (Epelboin, 1974); (*d*) most recent simulation on an IBM experimental teleprinter by Epelboin (1979). Progress in the time required for simulation: 42, 21 and 15 min for (*b*), (*c*) and (*d*) respectively.

A common characteristic apparent in all of the X-ray simulations examined so far is that the theoretically simulated image appears to underestimate the experimentally observed intensity in the region where the direct beam intersects the relevant defect (*i.e.* the direct image). All the experimental evidence shows considerably greater intensity in this region, as, for example, along *HI* in Fig. 6(*a*) for a stacking fault.

The reasons for the discrepancy in intensity between theory and experiment are not obvious. We enumerate various possible causes.

(1) For stacking faults there may, in addition to the displacement **u**, be other distortions giving rise to long-range strain fields which contribute to the intensity and have not been taken into account. Much is known (Patel, Jackson & Reiss, 1977) about the particular stacking faults we have studied and the presence of long-range strain fields seems doubtful for the following reasons: (*a*) Previous experiments (Maher, Staudinger & Patel, 1976) have revealed precipitate colonies associated with the center of these faults. These regions are of the order of microns in size at best and their strain fields are expected to drop off as $1/r^2$. The faults themselves are several hundreds of microns in size. Hence large regions of the fault should be out of range of the strain fields of the central colony of defects. When the fault sizes are smaller there is direct TEM evidence for large regions of precipitate-free faults (Maher, Staudinger & Patel, 1976). (*b*) If electrically active impurities on a scale not detectable by TEM are present in the vicinity of the fault plane, we expect these to be revealed by charge-collection scanning electron microscopy. With this technique (Kimerling, Leamy & Patel, 1977), however, we observe a temperature-dependent electrical contrast effect at the fault plane which can be attributed to the fault itself and not to an impurity.

(2) We examine briefly whether the theoretical approach used can underestimate the intensity observed experimentally. For planar defects the theoretical treatment of wave fields due to spherical waves makes use of the stationary-phase method to evaluate the integral representing the wave field in the crystal. This involves setting the first derivative of the phase factor $[\mathrm{d}G(s)/\mathrm{d}s] = 0$ [see p. 50 of Kato *et al.* (1967) for details]. The wave field in the diffracted-beam direction contains a second-derivative term $G''(s)$ in the denominator which is assumed to be large compared to $G'(s) = 0$. If we suppose that for some reason this condition does not hold and $G''(s)$ is small, the theoretical calculated intensity will be large. In other words if conditions exist where the assumptions in the stationary-phase method break down the theory should give a higher intensity. Our observations show that exactly the contrary is true and the theoretically calculated image displays relatively less intensity than the experimental section topograph. It is not possible at present to determine on the basis of the above simple arguments the origin of the excess intensity in the experimental section topographs. In particular, the actual theoretical problem is very complex since other assumptions, such as a slowly varying amplitude, are also explicit in the stationary-phase method. In any case extensive quantitative calculations would be necessary before any firm statements about the nature of the approximations can be made.

For other kinds of planar defects such as twins and grain boundaries the section-pattern simulations reveal the extreme sensitivity of the images to small changes in misorientation or displacement. Thus section topographs can be used as a very sensitive quantitative method for characterizing this class of planar defects. The details of twin and grain-boundary faults are discussed more fully by Katagawa and co-workers (in preparation). With regard to line defects, simple geometric criteria regarding visibility of dislocation contrast in X-ray topographs (Jenkinson & Lang, 1962) have long been used for establishing Burgers vectors of dislocations. In certain instances, for reasons not as yet completely clear, the simple geometric criteria give ambiguous results (Barns, Freeland, Kolb, Laudise & Patel, 1978). In such cases simulation methods for line defects demonstrated by Balibar & Authier (1967) and developed by Epelboin (1974) should prove invaluable in characterizing and identifying the observed dislocation contrast.

I thank N. Kato for clarifying the arguments for the calculated theoretical intensity using the stationary-phase method. It is a pleasure to acknowledge the assistance of P. E. Freeland with the experiments, and B. C. Wonsiewicz with the computing and simulation procedures.

References

AUTHIER, A. (1968). *Phys. Status Solidi*, **27**, 77–93.

AUTHIER, A. & PATEL, J. R. (1975). *Phys. Status Solidi A*, **27**, 213–222.

AUTHIER, A. & SAUVAGE, M. (1966). *J. Phys.* (*Paris*), **27**(*C*3), 137–150.

AZAROFF, L. V., KAPLOW, R., KATO, N., WEISS, R. J., WILSON, A. J. C. & YOUNG, R. A. (1974). *X-ray Diffraction*, pp. 295–298. New York: McGraw-Hill.

BALIBAR, F. & AUTHIER, A. (1967). *Phys. Status Solidi*, **21**, 413–422.

BARNS, R. L., FREELAND, P. E., KOLB, E. D., LAUDISE, R. A. & PATEL, J. R. (1978). *J. Cryst. Growth.* **43**, 676–686.

BEDYNSKA, T. (1973). *Phys. Status Solidi A*, **18**, 147.

BULLOUGH, R., MAHER, D. M. & PERRIN, R. C. (1971). *Phys. Status Solidi B*, **43**, 707.

EPELBOIN, Y. (1974). *J. Appl. Cryst.* **7**, 372–377.

EPELBOIN, Y. (1979). *Acta Cryst.* A**35**, 38–44.
HEAD, A. K., HUMBLE, P., CLAREBROUGH, L. M., FORWOOD, C. T. & MORTON, A. J. (1973). *Defects in Crystalline Solids*. Vol. 7. Amsterdam: North-Holland.
ISHIDA, H., MIYAMOTO, N. & KOHRA, K. (1976). *J. Appl. Cryst.* **9**, 240–241.
JENKINSON, A. E. & LANG, A. R. (1962). *Direct Observations of Imperfections in Crystals*, pp. 471–495. New York: Interscience.
KATAGAWA, T., ISHIKAWA, H. & KATO, N. (1975). *Acta Cryst.* A**31**, S246–S247.
KATO, N., KATAGAWA, T. & USAMI, K. (1967). *Adv. X-ray Anal.* **10**, 46–66.
KIMERLING, L. C., LEAMY, H. J. & PATEL, J. R. (1977). *Appl. Phys. Lett.* **30**, 217–219.
MAHER, D. M., STAUDINGER, A. & PATEL, J. R. (1976). *J. Appl. Phys.* **47**, 3813–3825.
PATEL, J. R. & AUTHIER, A. (1975). *J. Appl. Phys.* **46**, 118–125.
PATEL, J. R., JACKSON, K. A. & REISS, H. (1977). *J. Appl. Phys.* **48**, 5279–5288.
PATEL, J. R., WONSIEWICZ, B. C. & FREELAND, P. E. (1979). In preparation.
TAKAGI, S. (1962). *Acta Cryst.* **15**, 1311–1312.
WONSIEWICZ, B. C. & PATEL, J. R. (1976). *J. Appl. Phys.* **47**, 1837.

Acta Cryst. (1979). A**35**, 28–37

Dynamical Theory for Electron Scattering from Crystal Defects and Disorder*

BY J. M. COWLEY AND P. M. FIELDS

Department of Physics, Arizona State University, Tempe, Arizona 85281, *USA*

(*Received* 3 *April* 1978; *accepted* 5 *July* 1978)

Abstract

Dynamical diffraction calculations have been made by use of the periodic-continuation assumption for the diffuse scattering in electron diffraction patterns and for electron microscope images of single split interstitials in gold crystals for thicknesses up to 200 Å in order to demonstrate the strong fluctuations of scattering with thickness. The diffuse scattering from distributions of defects in crystals, described in terms of correlation functions, can be written in terms of 'dynamical factors' for each type of individual defect. These dynamical factors multiply the same Fourier transforms of correlation functions as are used in kinematical theory to give the effect of dynamical scattering on the diffraction intensities. Calculations of dynamical factors have been made by multi-slice dynamical diffraction methods for unit changes in atomic scattering factors and for atom displacements in gold and aluminum crystals in [001] orientation for thicknesses up to 100 Å. With increasing thickness the dynamical factors show rapidly reducing fluctuations with crystal thickness and become more nearly isotropic except for the effects of Kikuchi bands which are seen to develop.

* This paper was presented, by invitation, at the ACA Dynamical Diffraction Symposium held at the University of Oklahoma, 22 March 1978, honoring Paul P. Ewald on the occasion of his ninetieth birthday.

1. Introduction

Difficulties arise in the evaluation of electron scattering from defects and disorder in crystals because of the strong dynamical diffraction effects occurring even in very thin samples. While it is possible to write formal expressions for scattered amplitudes which are sufficiently accurate for the interpretation of any forseeable experimental observations with fast electrons (energy greater than about 20 keV), it is not in general feasible to make accurate calculations of the dynamical scattering effects for both the sharp Bragg reflections and the continuous background of diffuse scattering in diffraction patterns. The incentive to find approximate methods to deal with particular experimental situations has been considerable because of the significance of electron scattering methods for the study of perturbations of the periodicity of crystals, but as the power of the experimental methods has been increased the requirements for better approximations in the theoretical modelling have also been increased.

The use of a column approximation with, usually, a two-beam approximation and considerations limited to Bragg reflection amplitudes has served for much of the electron microscope study of dislocations and other extended crystal defects with medium-resolution imaging (10 Å or greater) for many years (Hirsch, Howie, Nicholson, Pashley & Whelan, 1965). Improved

00567-7394/79/010028-10$01.00